Int. J. Electrochem. Sci., 10 **(2015)** 9056 - 9072

International Journal of
ELECTROCHEMICAL
SCIENCE
www.electrochemsci.org

Corrosion Behavior of Aluminum Bronze under Thin Electrolyte Layers Containing Artificial Seawater

Y. Chen[1], *D.M. Qi*[2], *H.P. Wang*[3], *Z. Xu*[2], *C.X. Yi*[2], *Z. Zhang*[2,*]

[1]Department of Materials Science and Engineering, Zhejiang University, Hangzhou, Zhejiang 310027, China;
[2]Department of Chemistry, Zhejiang University, Hangzhou, Zhejiang 310027, China;
[3]Patent Examination Cooperation Center of the Patent Office, SIPO, Henan 450000, China;
[*]E-mail: eaglezzy@zjuem.zju.edu.cn

Received: 18 August 2015 / *Accepted:* 9 September 2015 / *Published:* 30 September 2015

The corrosion behavior of aluminum bronze under thin electrolyte layers (TELs) that contain artificial sea water has been investigated via Tafel polarization curve measurements, cathodic potentiodynamic curve measurements, electrochemical impedance spectroscopy (EIS), X-ray diffraction (XRD), scanning electron microscopy (SEM) and energy dispersive spectrometry (EDS). Tafel polarization curve showed that the corrosion rate increased with decreasing TEL's thickness at early stage, which is in good agreement with cathodic potentiodynamic curves and EIS measurements. However, after immersion for long periods of time, the corrosion rate varied non-monotonically with TEL thickness, at 302 μm＞202 μm＞403 μm＞bulk solution. The morphologies and EDS results demonstrated that aluminum bronze suffered a dealuminification corrosion and that the corrosion occurred initially at the interface between the α matrix and the β phase, before developing further within the β phase.

Keywords: aluminum bronze; thin electrolyte layer; atmospheric corrosion

1. INTRODUCTION

Aluminum bronze is a kind of copper alloys that are usually made up of copper, aluminum and some other additional elements such as manganese, iron, and nickel[1]. Because of its excellent mechanical properties, superior thermal and electrical conductivities, good resistance to corrosion and biofouling, relative ease of fabrication and low cost, aluminum bronze is widely applied in transistor systems, water treatment units, heat exchanger and shipboard condensers[2-7]. Aluminum bronze is more resistant to corrosion than pure copper and brass[8, 9] and their corrosion resistance was attributed to the formation of a film of $A1_2O_3$, which heals rapidly when damaged[10].The corrosion resistance increases with increasing aluminum content up to approximately 8% which is the limit of

the single α-phase[11]. Beyond this limit, two or more phase generates, which results in severe corrosion and serious loss in strength and ductility due to selective loss of aluminum[12]. In the past decades, a number of domestic and overseas scientific workers have extensively investigated the corrosion behavior of aluminum bronze in various aggressive medium [13-20].

Lorimer et al.[21] examined the short term corrosion behavior of four as-cast commercial aluminum bronzes in artificial sea water and pointed out that the corrosion rates of these phases were influenced by their volume fractions, morphologies and distributions in the microstructures. Zhang et al.[18] investigated the influence of microstructure on the corrosion behavior of three kinds of hot-extruded nickel aluminum bronze immersed in 3.5% NaCl solution and the results illustrated that the corrosion resistance of the alloy after annealing was improved due to the elimination of β martensite and ($\alpha+\kappa_{III}$) lamella eutectoid. For the quenched material, the corrosion rate was higher than that of the hot-extruded material because of an increase in the volume fraction of β phase that was anodic to α phase increased after quenching. Ateya et al.[12] studied the corrosion behavior of α-Albronze (Cu-7%Al) was in 3.4% NaC1 solution and found that the corrosive attack started very early, *ie*., during the first hour of immersion leading to general corrosion and pit nucleation, coalescence, growth, and eventual merging of neighboring pits together to give multiple trough-like cavities. The corrosion products were composed of a duplex film with an inner adherent layer of $A1_2O_3$ and an outer layer of Cu_2O, $Cu_2(OH)_3C1$, and Cu(OH)C1. However, all of these studies on corrosion of aluminum bronze were carried out in bulk solution system, but relatively few fundamental works involved in atmospheric corrosion. It is well known that a majority of metal serve in atmospheric environment, the atmospheric corrosion is the most universal spread form of corrosion, which occurs under thin electrolyte layers (TELs), or an adsorbed layer[22, 23]. The thickness of the TEL plays an important role in the process of atmospheric corrosion since the change in TEL thickness would influence mass transport of the dissolved oxygen, the hydration of dissolved metal ions and the accumulation of the corrosion products[24, 25]. In our previous work[26, 27], it was found that the corrosion rate of pure copper and tin bronze under TELs containing 3.5% NaCl increased with the decrease of TEL thickness during the initial stages, however, the corrosion behavior of aluminum bronze under different TELs is still not clear and the artificial seawater as the corrosive medium would provide more significant guidance for practical application.

In this paper, a series of electrochemical measurement techniques including Tafel polarization curve, cathodic potentiodynamic polarization and electrochemical impedance spectroscopy (EIS) were performed to investigate the corrosion behavior of aluminum bronze under various TELs containing artificial seawater in short and long term immersion. X-ray diffraction (XRD), scanning electron microscope (SEM) and energy dispersive spectrometer were employed to study the composition and morphology of corrosion products.

2. EXPERIMENTAL

2.1 Materials

The composition of aluminum bronze used in this study was determined by EDS with the result of Al 9.18% (wt.), Mn 1.74% (wt.), copper remained. The alloy was embedded into Teflon, leaving an

exposed surface area of 0.126 cm^2 as working surface. Prior to each experiment, the samples were abraded gradually from 400 to 1200 grit with the sand paper and polished with diamond paste down to 2.5 μm, then degreased in acetone, rinsed with double distilled water and finally dried in nitrogen gas. The electrolyte used in this study was artificial seawater (pH=7.68±0.01), prepared from analytical grade reagents and double-distilled water. The basic composition of the electrolyte is shown in Table 1.

Table 1. Chemical compositions of the employed artificial seawater

Species	Cl^-	SO_4^{2-}	CO_3^{2-}	Br^-	Na^+	Mg^{2+}	Ca^{2+}	K^+
mg/l	20237.2	3237.2	1066.3	72.9	11131.5	1366.6	650.4	423.0

2.2 TELs set-up

The experimental set-up used in this paper was the same as reported in our previous work[22, 28, 29]. The cell was fabricated and installed with high precision to assure that the electrolyte layer formed on the working electrode was even and stable. After polishing, the working electrode was firmly inserted into the cell. A platinum wire with a diameter of 0.3 mm was fixed around the working electrode and positioned below the exposed surface and used as the counter electrode; and saturated calomel electrode (SCE) connected through a salt bridge acted as reference electrode. The electrochemical cell mounted on a horizontal stage in vacuum desiccators can be adjusted to the horizontal level with a water level. The advantage of this arrangement is, even when the electrolyte layer on the working electrode is ultrathin, thereby minimizing the ohmic drop between the reference and working electrode.

The thickness of the electrolyte layer was determined by the device consisting of a sharp Pt needle and micrometer. According to the principle that the radii of the electrolyte layer have an obvious change when the sharp Pt needle touched the electrolyte surface caused by surface tension, the first value was recorded when the Pt-needle touched the working electrode surface, and the second was recorded when the obvious change in radii observed on the electrolyte surface. From the two micrometer values, the thickness of the layer can be calculated. This technique enabled the measurement of the TEL thickness with an accuracy of 10 μm. Over the course of experiment, the vacuum desiccator was completely covered with a lid and a small bottle of artificial seawater with the same concentration as the test solution was placed at the bottom of the vacuum desiccator to maintain the stability of the TEL thickness in the long term immersion.

2.3 Electrochemical measurements

The Tafel polarization and cathodic polarization measurements under various TEL thicknesses were performed on a commercial model 660A electrochemical workstation (CH Instruments Inc., US).

The Tafel polarization curve test was started from -0.12 V to 0.12 V with respect to the open circuit potential (OCP) at a sweep rate of 0.5 mV/s after immersion for 30 min. The cathodic potentiodynamic curve measurements was conducted from OCP to -1.6 V referred to SCE with the same sweep rate at 0.5 mV/s. EIS tests were performed using an impedance measurement unit (PARSTAT2273, Advanced Electrochemical System) over the frequency range of 100 k Hz -10 mHz at the OCP with a sinusoidal potential perturbation of 5 mV and the frequency sweep always started from high to low.

2.4 Characterization

The morphologies of corrosion products on the surface were observed by SEM (Hitachi SU 8000) equipped with an energy dispersive spectroscopy that can be used to measure the composition of corrosion products. To indentify the crystalline corrosion products of aluminum bronze after immersion for a long time, an ARL X'TRA X-ray diffractometer with CuK_{α} radiation (λ=0.15406 nm) was utilized at a scan rate of 3º/min.

3. RESULTS AND DISCUSSION

3.1Tafel polarization curve

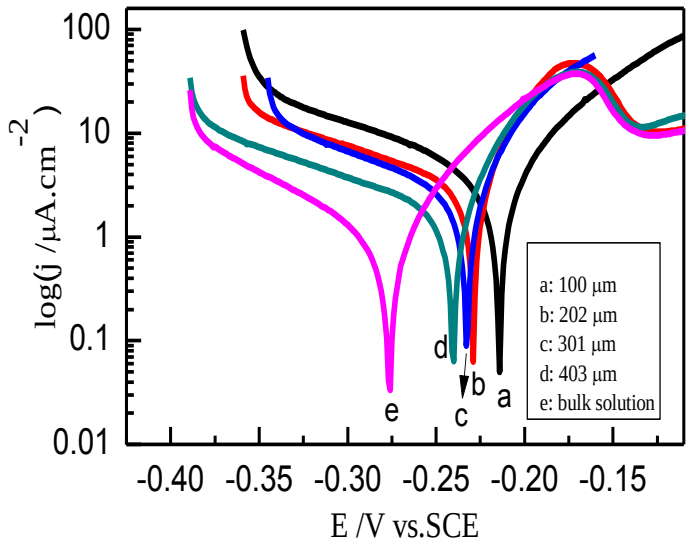

Figure 1. Tafel polarization curves of aluminum bronze under various thicknesses TEL

According to Tomashov's report[30], when the TEL thickness falls in the range of 1 μm ~ 1 mm, the atmospheric corrosion of metals is controlled by cathodic process. Meanwhile, when inspect of the polarization curves shown in Fig. 1, it is seen that all the curves are asymmetrical whose anodic branch are steeper than that of the cathodic branch, which also indicates that the cathodic process plays

a vital role in the corrosion process[31]. Because the anodic polarization under TELs was greatly affected by the surface state of working electrode and the current density was largely concentrated on the brim of the electrodes[27], only cathodic branch was fitting using the Tafel extrapolation method and the results are displayed in Table 2, where E_{corr} is the corrosion potential, j_{corr} is the corrosion current density at E_{corr} , b_a, b_c are the anodic and cathodic Tafel slope, respectively.

Table 2. The fitting results of polarization curves of aluminum bronze under TEL with various thicknesses.

Thickness(μm)	E_{corr}(V/SCE)	j_{corr}(μA/cm^2)	ba(mV/dec)	b_c(mV/dec)
100	-0.214	40.65	75.6	117
202	-0.229	19.06	69.8	140
301	-0.233	17.20	64.7	103
403	-0.240	15.56	61.5	134
bulk	-0.276	12.06	68.1	848

As shown in Table 2, the value of j_{corr} increase with the decrease of TELs thickness, which indicates the corrosion rate in the early stage increases with the decrease of TELs thickness, whereas the value of E_{corr} shifts towards positive values. The above results (Table 2) may be attributed to the higher transfer rate of O_2 across the thinner TEL film, which definitely accelerates the cathodic reactions that in turn speeds up the anodic corrosion process (based on Faraday rule).

3.2 Cathodic potentiodynamic curve

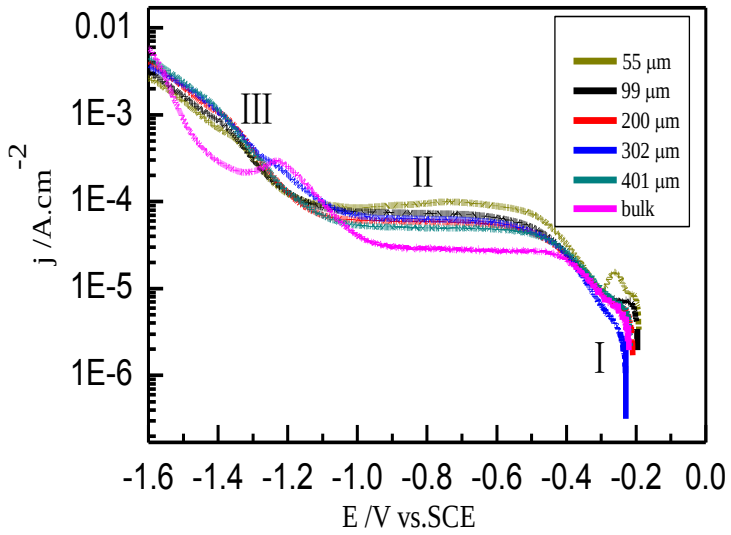

Figure 2. Cathodic potentiodynamic curves of aluminum bronze under TEL with different thicknesses

To confirm the effect of TEL thickness on the cathodic reaction rate, the cathodic potentiodynamic curve was carried out (Fig.2). All these cathodic potentiodynamic curves can be divided into three regions: region I in the vicinity of OCP is the weak polarization region; region II, at the more negative potential, attributes to the oxygen reduction under the diffusion process control, and region III corresponds to the hydrogen evolution. The small peak observed in region I may be ascribed to the reduction of corrosion product CuCl formed during the electrode equilibrium period[32, 33]. In region II, a distinct quasi-current-platform appeared that shows the characteristic of concentration polarization with a limited diffusion current (j_{lim}). In region III, cathodic current density increased rapidly and the Tafel slope also varied with the change of the TEL thickness.

The current densities at the midpoint potential of each straight line in Region II (Fig.2) are adopted to present the relationship of the TEL thickness with the corrosion current density (Fig.3). Fig.3 intuitively shows that j_{lim} decreases with the increase of TEL thickness, which is in good consistency with the corrosion behaviors of copper under the TELs containing Cl^- or SO_4^{2-} [26], respectively. However, when the TEL thickness exceeds 1000 μm, the change of j_{lim} with TEL thickness is negligible.

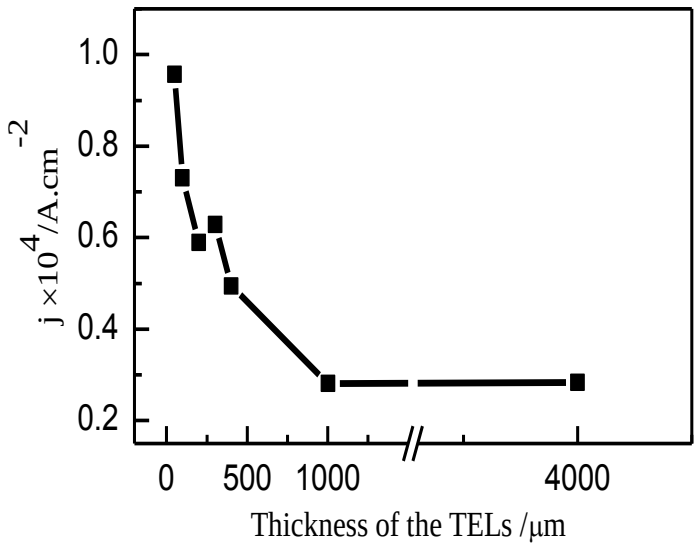

Figure 3. The cathodic polarization current densities taken at -0.8 V with various thickness

The main cathodic reaction occurred in regions I and II (Fig.3) is the reduction of oxygen (Eq. (1))[34], and reaction rate is controlled by the diffusion of the reactant oxygen from bulk solution to electrode surface.

$$O_2 + 2H_2O + 4e \rightarrow 4OH^- \qquad (1)$$

The diffusion process of oxygen through the TEL films has been generally considered to be one-dimensional and described by the Nernst-Fick equation[24] (Eq. (2))

$$i_{\lim,O_2} = \mathrm{nFD}_{O_2}[O_2]/\delta \qquad (2)$$

where n is the electron number participated in the oxygen reduction reaction, F is the Faraday constant, D_{O2} and $[O_2]$ are the diffusion coefficient and oxygen concentration in the electrolyte layer, respectively and δ is the thickness of diffusion layer.

According to Eq.2, $j_{lim,O2}$ is inversely proportional to the TELs thickness which has also been proved by the results of cathodic potential dynamic curves. However, when the TELs are sufficiently thick, they consists of two parts: an inner diffusion layer and an outer convection layer; once the change of TEL thickness occurs in the convection layer, the value of $j_{lim,O2}$ should stay constant[22]. This is a convincing explanation for the behavior of very thick TELs (δ> 1000 μm).

3.3 The effect of oxygen on cathodic reaction

Based on the above discussion, it can be seen that the cathodic reaction is the rate-controlling step in atmospheric corrosion. As the main reactant, the content of oxygen may have an important influence on the cathodic reaction, therefore a series of cathodic potentiodynamic curve measurements were carried out in bulk solution, the results of which are displayed in Fig.4.

From Fig.4 we can see that the open circuit potential moves to positive direction when the bulk solution changed from N_2 saturation to O_2 saturation, and that the value of i_{lim} is greater which is a good way to confirm the previous conclusion that the thinner the TELs, the faster the cathodic reaction. In view of the two characteristic namely, the i_{lim} is constant within a certain range of potential and there is a positive correlation between i_{lim} and oxygen content, we can safely draw the conclusion that diffusion process of oxygen is the main rate-controlling step in cathodic reaction[35].

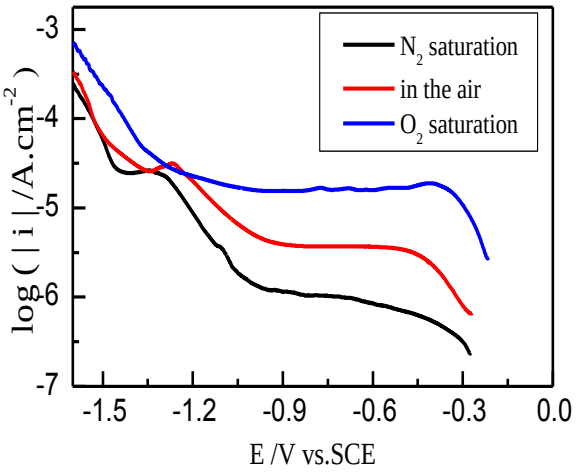

Figure 4. Cathodic potentiodynamic curves of aluminum bronze in bulk solution with different oxygen

3.4 EIS measurements

The EIS measurements of aluminum bronze in artificial sea water under various TELs were monitored and the results are displayed in Fig.5. It can be seen that the Nyquist plot in initial stage of

corrosion for all TELs were composed of two capacitive arcs at high and intermediate frequencies (HFs and MFs) and a tail at low frequencies (LFs). The capacitive loop at HFs corresponds to the solution resistance and corrosion product film resistance. The diameter of MFs capacitive arc is associated with the charge-transfer resistance [31] and the tail at LFs corresponds to the Warburg impedance which relates to a diffusion process [36]. This diffusion process results from the transport of oxygen through the solution to reaction interface. Another point worth noting is, the diameter of capacitive arcs increased with the increase of TELs thickness in the early and middle stage of corrosion (seen by referring to Fig. 5 A and B) which indicates the electrochemistry reaction proceeds faster at lower TELs thickness. However, with the immersion time prolonged further, corrosion process altered gradually due to the accumulation of corrosion products and the attack of aggressive ions as shown in Fig.5 C. Two capacitive arcs and Warburg impedance still existed (except in the case of corrosion in bulk solution), but the diameter of capacitive arcs under various TELs thickness decreased in the following order: 302 μm＞202 μm＞403μm＞bulk solution (in the later period, the solution resistance of 105 μm became very large and the corrosion rate was not compared with others, so it isn't listed here).

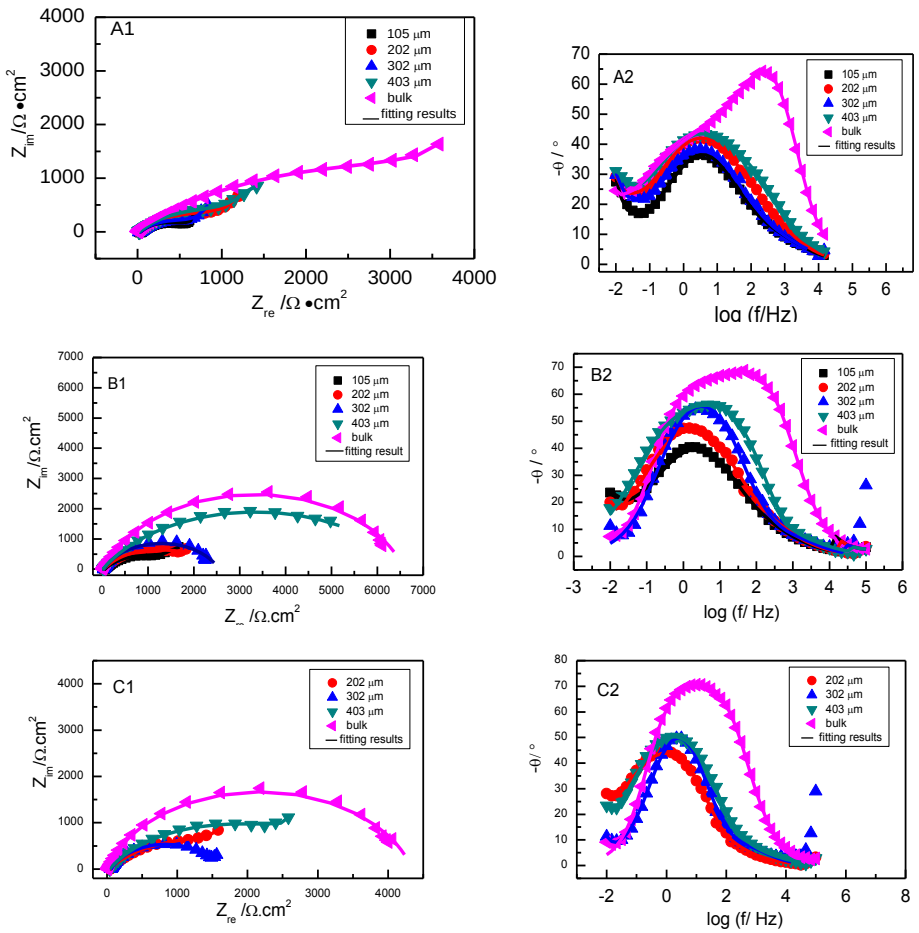

Figure 5. EIS plots of aluminum bronze under TEL with various thicknesses at different immersion time (A for 0.5 h; B for 168 h; C for 384 h)

To explore the variation of corrosion behavior with different immersion time in-depth, a specific TEL thickness at 302 μm was chosen to display in Fig.6. As mentioned before, the tail aroused

at LFs in initial stage disappeared with the propagation of immersion time, but occurred again during the later immersion. The increase of capacitive loop diameter evinced that the corrosion product layer was thickened and the protection performance of the corrosion layer had improved, since the concentration of artificial seawater used in this paper was relatively high, the corrosion product layer could not resist the attack of aggressive ions and broke down partially, thus we can see that the size of the capacitive arc decreased and the Warburg impedance appeared again in the later stage [37].

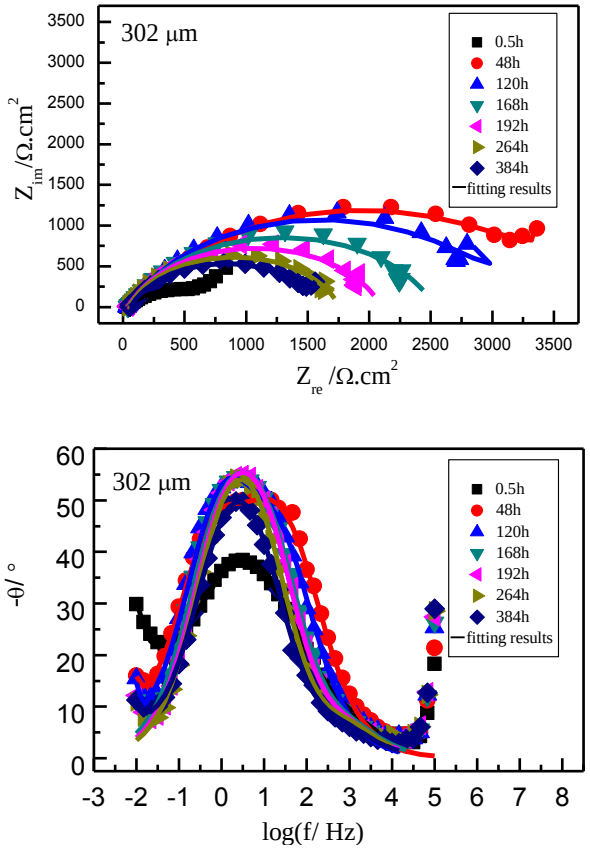

Figure 6. EIS plots for aluminum bronze depending on immersion time at 302 μm

To account for the diffusion process, the impedance data were analyzed using two different equivalent electrical circuits shown in Fig. 7. The first (Fig. 7a) was used to fit the EIS data with a Warburg impedance, and the second (Fig. 7b) was for the EIS data with only two capacitive loops. In these circuits, R_s represents the solution resistance, R_f is the sum of film resistances of corrosion products, R_{ct} is the charge transfer resistance and W_1 is the Warburg diffusion impedance. CPE_1 and CPE_2 represent the constant phase angle element of corrosion products and double-layer locating in the reaction interface, respectively. The presence of *CPE* has been explained by dispersion effects that caused by microscopic roughness of a solid surface [38, 39]. Some typical fitting parameters obtained from equivalent circuits are listed in Table 3-6.

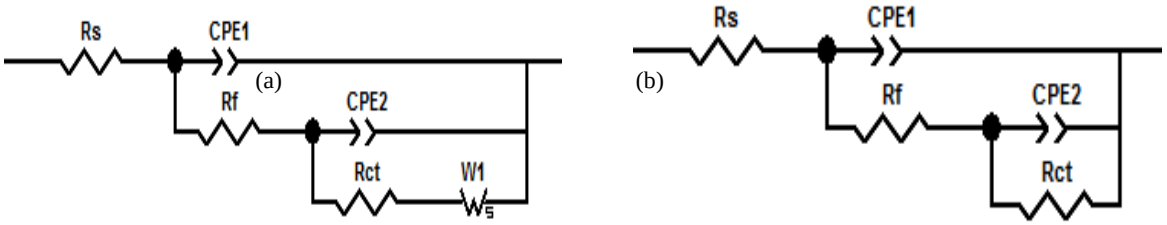

Figure 7. Equivalent circuits used for simulating the experimental impedance data for aluminum bronze covered with electrolyte layers containing artificial seawater

Table 3. Fitting results of EIS for aluminum bronze with various thicknesses immersion for 0.5 h

Parameters	105 μm	202 μm	302 μm	403 μm	bulk
$R_s/(\Omega \cdot cm^2)$	30.32	21.91	26.09	16.24	4.92
$CPE_1/(\mu F \cdot cm^{-2})$	315.87	636.51	365.87	399.21	39.13
n_1	0.65	0.61	0.64	0.65	0.90
$R_{surf}/(\Omega \cdot cm^2)$	23.99	112.58	17.30	71.47	149.06
$CPE_2/(\mu F \cdot cm^{-2})$	692.14	227.78	680.95	480.95	391.27
n_2	0.63	0.66	0.60	0.56	0.52
$R_{ct}/(\Omega \cdot cm^2)$	589.68	1033.96	720.72	1405.66	5008.50
$R_{surf}+ R_{ct}/(\Omega \cdot cm^2)$	613.67	1146.54	738.02	1477.12	5157.56

Table 4. Fitting results of EIS for aluminum bronze with various thicknesses immersion for 168 h

Parameters	105 μm	202 μm	302 μm	403 μm	bulk
$R_s/(\Omega \cdot cm^2)$	53.49	34.05	36.40	24.22	5.26
$CPE_1/(\mu F \cdot cm^{-2})$	303.17	328.51	91.27	346.03	105.56
n_1	0.65	0.67	0.78	0.65	0.84
$R_{surf}/(\Omega \cdot cm^2)$	45.81	31.73	14.44	15.38	1094.31
$CPE_2/(\mu F \cdot cm^{-2})$	340.26	367.86	222.22	17.78	56.43
n_2	0.62	0.65	0.59	0.98	0.80
$R_{ct}/(\Omega \cdot cm^2)$	1456.18	2145.91	2488.63	6667.29	5476.72
$R_{surf}+ R_{ct}/(\Omega \cdot cm^2)$	1502.00	2177.63	2503.67	6682.67	6571.03

Table 5. Fitting results of EIS for aluminum bronze with various thicknesses immersion for 384 h

Parameters	202 μm	302 μm	403 μm	bulk
$R_s/(\Omega \cdot cm^2)$	44.50	51.32	35.65	5.58
$CPE_1/(\mu F \cdot cm^{-2})$	1103.17	105.56	424.60	137.30
n_1	0.60	0.77	0.63	0.84
$R_{surf}/(\Omega \cdot cm^2)$	52.45	19.78	18.31	12.24
$CPE_2/(\mu F \cdot cm^{-2})$	46.11	288.10	165.08	41.67
n_2	0.96	0.77	0.75	0.82
$R_{ct}/(\Omega \cdot cm^2)$	2182.07	1535.06	3216.53	4322.05
$R_{surf} + R_{ct}/(\Omega \cdot cm^2)$	2234.52	1554.84	3234.84	4334.29

According to the fitting results, the value of R_s is quite small, which demonstrate that the ohmic drop between working electrode and reference electrode was minimized effectively. The value of *n* concentrated in the range 0.6 to 0.8, which indicate that the electrode surface is heterogeneous, otherwise the *n* would closed to 1. The fluctuation of CPE_2 results from the change of real area on the corroded electrode during corrosion process[40]. The most important parameter R_{ct} can be used to evaluated the corrosion rate on condition that there are two or multiple variables affecting corrosion process in addition to potential, or else the polarization resistance (R_p) is also applicable[41].

Table 6. The EIS fitting results of aluminum bronze with different immersion time at the 302 μm

Parameters	0.5 h	48 h	120 h	168 h	192 h	264 h	384 h
$R_s/(\Omega\cdot cm^2)$	26.09	30.52	33.45	36.40	36.41	40.55	51.32
$CPE_1/(\mu F\cdot cm^{-2})$	365.87	208.73	269.84	91.27	92.06	80.16	105.56
n_1	0.64	0.74	0.74	0.78	0.79	0.79	0.77
$R_{surf}/(\Omega\cdot cm^2)$	17.30	946.13	900.27	14.44	14.39	15.96	19.78
$CPE_2/(\mu F\cdot cm^{-2})$	680.95	175.40	74.29	222.22	235.71	276.98	288.10
n_2	0.60	0.80	0.94	0.75	0.77	0.79	0.77
$R_{ct}/(\Omega\cdot cm^2)$	720.72	2667.67	2235.62	2488.63	2051.41	1705.91	1535.06
$R_{surf}+R_{ct}$	738.02	3613.81	3135.89	2503.07	2065.80	1721.88	1554.84

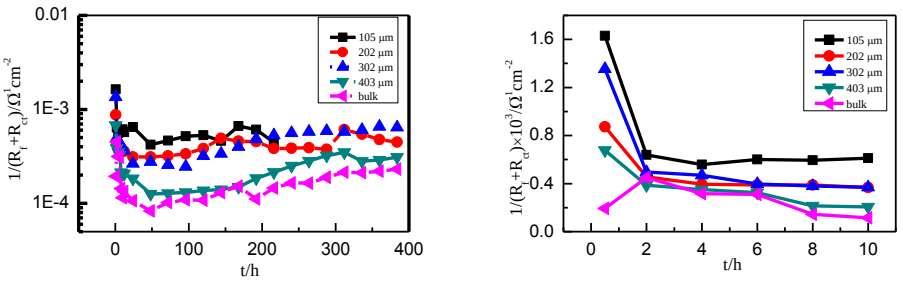

Figure 8. Variation of corrosion rates for aluminum bronze with immersion time under different TEL thicknesses

In this paper, two time constants at HFs and MFs overlapped leading to R_f and R_{ct} are not well distinguished. Therefore, the sum of R_f and R_{ct} is used to represent corrosion resistance, the larger the sum value, the slower the corrosion rate. The reciprocal of the sum of R_f and R_{ct} as a function of the immersion time is plotted in Fig. 8. It can be seen that the corrosion rate during short-term exposure decreased in the sequence of 105 μm＞302 μm＞202 μm＞403 μm＞bulk solution which was in good agreement with the results of cathodic potential dynamic curves. With the extension of immersion time, the corrosion rate ordering changed to 302 μm＞202 μm＞403 μm＞bulk solution. The reason may be that, considerably more corrosion products accumulated on the electrode surface during the long immersion time and it's far easier for the corrosion products and metal ions diffused from the

electrode surface into solution in a relatively thick electrolyte layers. Although the corrosion process is still controlled by the cathodic reaction, the rate-determining step of the cathodic reaction is transformed from O_2 diffusion to electrochemical reaction firstly evidenced by the disappearance of Warburg impedance and then to O_2 diffusion due to the Warburg impedance arose again[26], as a consequence, the corrosion rate on 302 μm is higher than that in bulk solution and 403 μm owing to higher O_2 concentration. When the TEL was less than 302 μm, the anodic process was inhibited because the diffusion of chloride ions and corrosion products in the thinner TELs became harder. Referred to Tomashov's model[30], there is a critical thickness at the point of the transition from cathodic to anodic control; such that a maximum corrosion rate can be achieved which corresponds to the 302 μm in this paper.

3.5 Characterization

Fig. 9 shows the XRD patterns of aluminum bronze before and after corrosion for 384 h immersion in artificial seawater under various TEL thickness. The peaks corresponding to α copper and of metastable β copper can be found in diffraction patterns of the uncorroded sample and the composition is α-Cu (solid solution of Al in Cu) and Cu3Al respectively. However, the intensity of the main diffraction peaks corresponding to α-Cu and Cu3Al decreased and some new diffraction peaks appeared after corrosion in the long term. These new diffraction peaks represented corrosion products cuprite (Cu_2O), aluminum oxide (Al_2O_3), cuprous chloride (CuCl), aluminum chloride hydroxide [Al2(OH)5Cl], atacamite [Cu2(OH)3Cl] and malachite [$Cu_2(OH)2CO_3$] respectively which are in agreement with those reported in the literature[12, 42-45]. Although some hydroxyl sulfide such as $Cu_4(OH)_6SO_4$ and $Al_4SO_4(OH)10{\cdot}4H_2O$ [42, 44] are reported as the corrosion products in the long term exposure in environment containing SO42- , they are not found in the XRD figures due to the low abundance and amorphous structure. Another new peaks closed to α-Cu represent pure copper which is generated by dealuminification of metastable β phase .

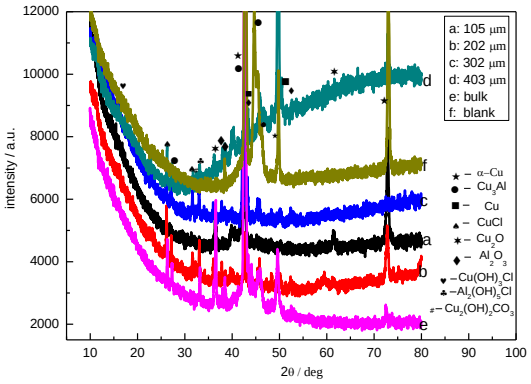

Figure 9. XRD patterns of Aluminum bronze before and after 384 h immersion

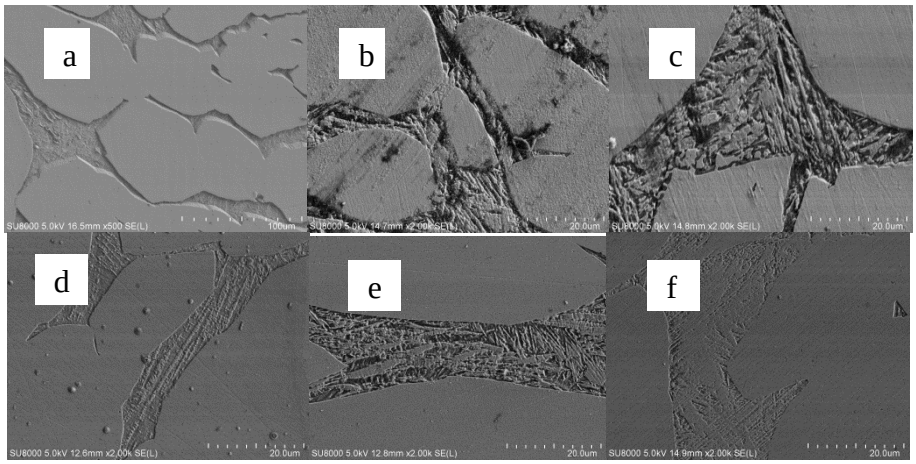

Figure 10. SEM images of the aluminum bronze surface after etched (a) and 3 h immersion time in artificial seawater (b) 102μm, (c) 198μm, (d) 302μm, (e) 401μm and (f) in the bulk solution

To examine the microstructure of aluminum bronze, the sample was etched in a solution of 0.5 g $FeCl_3$ and 0.5 ml HCl in 10 ml H_2O after being mechanically abraded and polished. Two different phase (*i.e.* the α and β eutectoid) were clearly shown in Fig. 10(a) and the element content in different areas are given in Table. 7. It is obvious that the aluminum content in β phase is higher than α phase. Based on the reports[11, 13], the β phase is more active than α phase and the corrosion normally occurred first at the interface of the α matrix and the β phase, then develops within the β phase which can be verified in Fig.10 (b)-(f). The distinctive grain boundaries between α and β phase after immersion 3 h under various thickness of electrolyte layers indicates the phase interface corroded preferentially. However, when the immersion time was prolonged to 384 h, we can see in visualization a layer of loose powdery scale of a light bluish green color covered the entire surface of working electrode at ca. 200, 300 and 400 μm while the reddish brown with small greenish stains and little powdery patina observed for 100 μm. Since the diffusion of corrosion products and metal ions is quickly enough, the surface of sample immersed in bulk remained bright yellow color.

The more subtle morphology was found via SEM and displayed in Fig. 11. It can clearly be seen that the aluminum bronze after immersion in artificial seawater for 384 h suffered serious damage. The outermost layer bluish green powdery was fluffy spherical spongiform (Fig.11 a) and their compositions might be primarily $Cu(OH)Cl_3$ 、 $Cu_2(OH)_2CO_3$ 、 $Cu_4(OH)_6SO_4$ 、 $Al_4SO_4(OH)_{10}{\cdot}4H_2O$、$Al_2(OH)_5Cl$ combined the EDS results in Table 7 with the XRD results. The second layer was revealed by gently removing the outermost layer corrosion products with a brush, showing a microstructure consisting of fine acicular or flocculent which might be consisted of Cu_2O, CuCl [20]. The innermost layer corrosion product with a plate structure can be found in the crack gap which was identified as $A1_2O_3$ (in Fig.12a) [12].

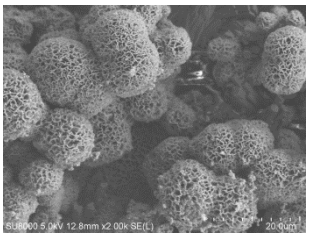

A

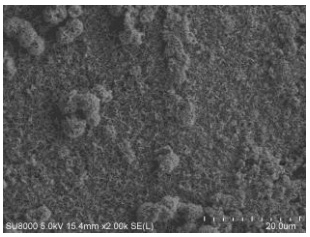

B

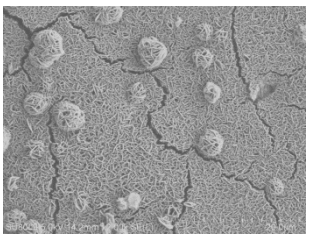

C

Figure 11. SEM images of the corrosion products on the surface of aluminum bronze surface after immersion for 384 h in artificial seawater (a) the outermost layer corrosion products, (b-c) the second layer corrosion products (b): 302 μm, (c): in the bulk solution

Table 7. EDX analysis of different corrosion products layer in the corroded aluminum bronze (mass concentration, wt.%)

Element (wt%)	Cu	Al	O	Cl	C	S
The outermost layer	38.81	9.98	42.37	4.33	1.94	2.57
The second layer in 302 μm	44.50	11.57	43.01	0. 917	---	---
The second layer in bulk solution	49.80	12.33	36.55	1.31	---	---

Table 8. EDX analysis of different areas in the corroded aluminum bronze (mass concentration, wt.%)

element	Mass concentration (wt.%)		
	α-phase	β-phase	corroded areas
Cu	90.38	73.70	98.00
Al	8.31	12.06	0.32

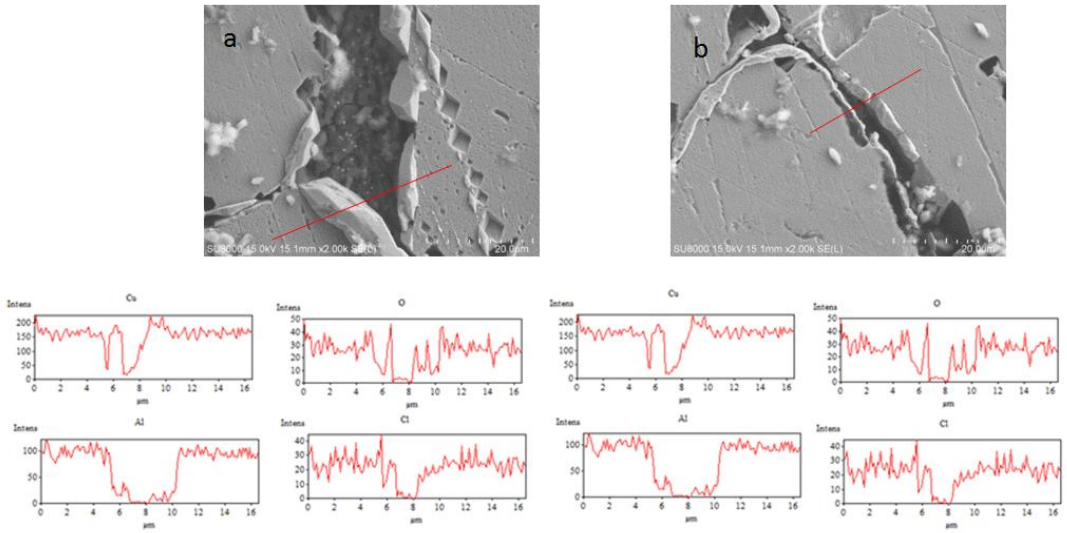

Figure 12. The micrograph of the innermost layer corrosion product in the crevice gap. (a) and the surface morphology with crevices (b) and the element distribution, respectively in fastline-scan mode

From the SEM image, we can see the surface structure of corrosion products are not compact which can allow a passage for aggressive ion and oxygen diffusion and lead to the corrosion accelerated. The crevices with a width of 4~18 μm and the EDS results displayed in Table 8 and Fig. 12b demonstrated that the aluminum bronze suffered a dealuminification attack primarily because of the lower aluminum content and higher copper content in the corroded areas than that of the uncorroded areas and the attack occurred initially at the interface of the α matrix and the β phase, and developed within the β phase, ultimately leading to the crevices generated in β phase after immersion for 384 h.

4. CONCLUSION

The corrosion behavior of aluminum bronze under thin electrolyte layers (TELs) is quite different from that in bulk solution. Polarization results showed that the corrosion rate increased with the decrease of TEL's thickness during the early stage of corrosion which is in good accordance with the results of EIS. The corrosion rate in this period was controlled by oxygen diffusion. However, after a long period of immersion, during which more corrosion products accumulated on the surface of electrode, it was easier for the corrosion products and the metal ions to diffuse from the electrode surface into solution in a relatively thick electrolyte layers, leading to the corrosion rate varying with thickness in the sequence 302 μm＞202 μm＞403 μm＞bulk solution. The corrosion products after exposed in artificial seawater in the long term appear as a multi-layered structure with an innermost layer of $A1_2O_3$ and the second layer of Cu_2O and CuCl and the outermost layer of $Cu(OH)Cl_3$、$Cu_2(OH)_2CO_3$、$Cu_4(OH)_6SO_4$、$Al_4SO_4(OH)_{10}\cdot 4H_2O$、$Al_2(OH)_5Cl$. The results of SEM and EDS

demonstrated that aluminum bronze suffered dealuminification corrosion and that the corrosion occurred initially at the interface of the α matrix and the β phase, then developed within the β phase.

ACKNOWLEDGEMENTS
The authors wish to acknowledge the financial supports of the National Natural Science Foundation of China (Project 21403194, 21273199) and Zhejiang province Postdoctoral Science Foundation (Grant No. BSH1402021).

References

1. L. W. Gleekman, R.K. Swandby, *Corrosion*, 17 (1961) 116.
2. B.S. Yilbas, A. Matthews, A. Leyland, C. Karatas, S.S. Akhtar, B.J. Abdul Aleem, *Appl. Surf. Sci.* 263 (2012) 804.
3. A. Al-Hashem, P.G. Caceres, W.T. Riad, H.M . Shalaby, *Corrosion*, 51 (1995) 331.
4. E.A.Ashour, L.A. Khorshed, G.I. Youssef, H.M. Zakria, T.A. Khalifa, *Mater. Sci. Appl*, 5 (2014) 10
5. M. Kaplan, A.K. Yildiz, *Mater. Lett*, 57 (2003) 4402.
6. S. Neodo, D. Carugo, J.A. Wharton, K.R. Stokes, *J. Electroana. Chem.* 695 (2013) 38.
7. F.X. Chen, H.J. Li, J.Q. Guo, Y.S. Yang, *Mater. Sci. Eng., A,* 499 (2009) 315.
8. J.A. Wharton, R.C. Barik, G. Kear, R.J.K. Wood, K.R. Stokes, F.C. Walsh, *Corros. Sci.* 47 (2005) 3336.
9. A. V. Benedti, P.T.A.Sumodjo, K. Nobe, P. L. Cabot, W. G. Proud, *Electrochim. Acta*, 40 (1995) 2657.
10. X.F. Zhang, L. Fang, *Wear*, 253 (2002) 1105.
11. Z. Han, H. Zhao, *Mater. Sci. Eng., A,* 345 (2003) 8.
12. B.G.Ateya, *J. Electrochem. Soc*, 141 (1994) 71.
13. Z. Han, Y.F. He, H.C. Lin, H. Zhao, *J. Mater. Sci. Lett*, 19 (2000) 393.
14. W.S. Li, Z.P. Wang, Y. Lu, Y.H. Jin, L.H. Yuan, F. Wang, *Wear,* 261 (2006) 155.
15. A. Schüssler,H.E. Exner, *Corros. Sci*, 34 (1993) 1803.
16. W.A. Badawy, R.M. El-Sherif, H. Shehata, *J. Appl. Electrochem*, 37 (2007) 1099.
17. A. Al-Hashem, W. Riad, *Mater. Charact.* 48 (2002) 37.
18. D. Zhang, R. Chen, W. Zhang, *Acta. Metall. Sin*, 23 (2010) 113.
19. E.A.Ashour, *J. Mater. Sci*, 36 (2001) 201.
20. E.A.Ashour, B.G. Ateya, *Electrochim. Acta*, 42 (1997) 243.
21. G. W. Lorimer, F.Hasan, J. Iqbal, N. Ridley, *Br. Corros. J.*, 21 (1986) 244.
22. Y.L.Cheng, Z. Zhang, F.H. Cao, J.F. Li, J.Q. Zhang, J.M. Wang, C.N. Cao, *Corros. Sci*, 46 (2004) 1649.
23. H. Huang, X. Guo, G. Zhang, Z. Dong, *Corros. Sci*, 53 (2011) 1700.
24. A. Nishikata, Y. Ichihara, Y. Hayashi, T. Tsuru, *J. Electrochem. Soc*, 144 (1997) 1244.
25. G.A. El-Mahdy, A.K.F. Dyab, H.A. Al-Lohedan, *Int. J. Electrochem. Sci.,* 8 (2013) 5232.
26. X.N. Liao, F.H. Cao, L.Y. Zheng, W.J. Liu, A.N. Chen, J.Q. Zhang, C.N. Cao, *Corros. Sci*, 53 (2011) 3289.
27. X.N. Liao, F.H. Cao, A.N. Chen, W.J. Liu, J.Q. Zhang, C.N. Cao, *T. Nonferr. Metal. Soc*, 22 (2012) 1239.
28. W.J. Liu, F.H. Cao, A.N. Chen, L.R. Chang, J.Q. Zhang, C.N. Cao, *Corros. Sci*, 52 (2010) 627.
29. W.J. Liu, F.H. Cao, B.L. Jia, L.Y. Zheng, J.Q. Zhang, C.N. Cao, X.G. Li, *Corros. Sci*, 52 (2010) 639.
30. N.D.Tomashov, *Corrosion*, 20 (1964) 7.

31. W.J. Liu, F.H. Cao, L.R. Chang, Z. Zhang, J.Q. Zhang, *Corros. Sci*, 51 (2009) 1334.
32. C. Deslouis, B. Tribollet, G. Mengoli, M.M. Musiani, *J. Appl. Electrochem*, 18 (1988) 374.
33. C. Deslouis, B. Tribollet, G. Mengoli, M.M. Musiani, *J. Appl. Electrochem*, 18 (1988) 384.
34. F. King, M.J. Quinn,C.D. Litke, *J. Electroanal. Chem*, 385 (1995) 45.
35. L. Di, *Electrochemistry principle*, Beijing: Beihang University Press, 2008.
36. Y. Van Ingelgem, E. Tourwé, J. Vereecken, A. Hubin, *Electrochim. Acta*, 53 (2008) 7523.
37. R.P.B.Hernández, Z. Pászti, H.G. de Melo, I.V. Aoki, *Corros. Sci*, 52 (2010) 826.
38. Z. Zhang, J.Q. Zhang, J.M. Wang, C.N. Cao, *Chin. J. Nonferr. Met*, 11 (2001) 284.
39. J.U.Chavarin, *Corrosion*, 47 (1991) 472.
40. E.B. Castro, C.A. Gervasi, *Int. J. Hydrogen Energy*, 25 (2000) 1163.
41. I. Epelboin, M. Keddam, H. Takenouti, *J. Appl. Electrochem*, 2 (1972) 71.
42. A. Krätschmer, I.O.Wallinder, C. Leygraf, *Corros. Sci*, 44 (2002) 425.
43. A. M. Beccaria, E.D.Mor, G. Poggi, F. Mazza, *Corros. Sci*, 27 (1987) 363.
44. D.B.Blücher, J.E. Svensson, L.G. Johansson, *Corros. Sci*, 48 (2006) 1848.
45. L. Núñez, E. Reguera, F. Corvo, E. González, C. Vazquez, *Corros. Sci*, 47 (2005) 461.